J. Fluid Mech. (2010), *vol.* 653, *pp.* 365–390.
doi:10.1017/S0022112010000388

Optimization of pulsed jets in crossflow

RAJES SAU AND KRISHNAN MAHESH†
Aerospace Engineering and Mechanics, University of Minnesota, Minneapolis, MN 55455, USA

(Received 13 August 2009; revised 15 January 2010; accepted 16 January 2010;
first published online 21 April 2010)

We use direct numerical simulation to study the mixing behaviour of pulsed jets in crossflow. The pulse is a square wave and the simulations consider several jet velocity ratios and pulse conditions. Our objective is to study the effects of pulsing and to explain the wide range of optimal pulsing conditions found in experimental studies of the problem. The central theme is that pulsing generates vortex rings; the effect of pulsing on transverse jets can therefore be explained by the behaviour of vortex rings in crossflow. Sau & Mahesh (*J. Fluid Mech.*, vol. 604, 2008, pp. 389–409) show that vortex rings in crossflow exhibit three distinct flow regimes depending on stroke and ring velocity ratios. The simulations of pulsed transverse jets in this paper show that at high velocity ratios, optimal pulse conditions correspond to the transition of the vortex rings produced by pulsing between the different regimes. At low velocity ratios, optimal pulsing conditions are related to the natural time scale on which hairpin vortices form. An optimal curve in the space of stroke and velocity ratios is presented. Data from various experiments are interpreted in terms of the properties of the equivalent vortex rings and shown to collapse on the optimal curve. The proposed regime map allows the effects of experimental parameters such as pulse frequency, duty cycle, modulation and pulse energy all to be predicted by determining their effect on the equivalent stroke and velocity ratios.

1. Introduction

Jets in crossflow are central to applications such as dilution holes in combustors, fuel injectors, pollutant dispersion from smoke stacks, thrust vectoring of turbojets and V/STOL aircraft. A large body of work therefore exists (see e.g. the review by Margason 1993). There have been some attempts to develop control strategies for this flow. Recent experiments (e.g. Wu, Vakili & Yu 1988; Chang & Vakili 1995; Hermanson, Wahba & Johari 1998; Johari, Pacheco-Tougas & Hermanson 1999; Blossey *et al.* 2001; Eroglu & Breidenthal 2001; M'Closkey *et al.* 2002; Karagozian, Cortelezi & Soldati 2003; Shapiro *et al.* 2006) have considered periodic pulsed excitation of the jet as a means of control and shown that jet penetration and spread can be maximized under specific pulsing conditions. The pulsing mechanism has involved solenoidal valves (Eroglu & Briedenthal 2001), spinning mechanical valves (Narayanan, Barooah & Cohen 2003) and acoustic forcing (Vermuelen, Rainville & Ramesh 1992; M'Closkey *et al.* 2002; Shapiro *et al.* 2003). The effects of forcing amplitude, duty cycle (defined as the fraction of time during a period that the pulsing is 'on') and shape of forcing waveform have been considered.

† Email address for correspondence: mahesh@aem.umn.edu

The following observations have been made. Square wave excitation is more effective than sinusoidal forcing (M'Closkey *et al.* 2002). We therefore consider square wave excitation in this paper. Forcing at frequencies that are dominant near the jet exit does not cause appreciable change in jet penetration. Also, while mixing might be enhanced locally, peak scalar levels in the far field remain high (Narayanan *et al.* 2003). Low frequency forcing yields significant increase in jet penetration depth (Wu *et al.* 1988; Johari *et al.* 1999; Eroglu & Briedenthal 2001; M'Closkey *et al.* 2002; Narayanan *et al.* 2003). Optimal forcing conditions are configuration- and apparatus-dependent (Shapiro *et al.* 2003). Also, the optimal frequencies vary over a wide range (Narayanan *et al.* 2003). In general, as long as the forcing frequency is low enough, an optimal duty cycle is found to exist (Shapiro *et al.* 2003). Pulsing might have a greater effect on mixing at low velocity ratios and lower Reynolds numbers (Eroglu & Briedenthal 2001). Long injection times yield moderate enhancement for fully pulsed jets, while short injection times and smaller duty cycle yield significant enhancement over the steady jet (Johari *et al.* 1999).

The physical mechanisms that maximize jet penetration are not well understood; also, scaling laws that allow optimal conditions to be predicted/scaled are not known. The optimal conditions are typically presented in terms of a Strouhal number, St. However, the optimal St can vary from 0.004 to 0.5 between experiments (Narayanan *et al.* 2003). Some researchers (e.g. M'Closkey *et al.* 2002; Shapiro *et al.* 2003; Johari 2006) relate optimal pulse condition for maximum penetration to the 'formation number' proposed by Gharib, Rambod & Shariff (1998) for vortex ring formation in a quiescent medium. Formation number which is a universal time scale, denotes the transition between two distinct states of vortex rings in stationary fluid – single vortex ring and vortex ring with trailing column. Johari (2006) proposes 'stroke ratio' and 'duty cycle' as the only parameters describing pulsed jets in crossflow. A classification scheme is proposed which is based on the 'formation number'. He suggests that discrete vortex rings are created for $L/D < 4$ and rings with trailing column are produced for $L/D > 4$. However, Sau & Mahesh (2008) show that this is only valid in a quiescent medium; crossflow significantly changes the vortex ring dynamics and mixing properties. Three regimes for vortex rings are found and transition between these regimes strongly depends on the crossflow velocity ratio. The scaling used by Johari (2006) is only based on vortex ring properties in stationary fluid. The effect of crossflow, i.e. jet to crossflow velocity ratio, on the vortex rings is ignored. Furthermore, the critical stroke ratio for deeply penetrating vortical structures and optimal jet penetration is approximately one-half of the 'formation number' (M'Closkey *et al.* 2002; Shapiro *et al.* 2003). There have been attempts to relate the pulsing to shear-layer instabilities in the jet. Megerian *et al.* (2007) studied the effect of jet velocity ratio R on shear-layer instabilities in transverse jets. The nature and strength of the instability modes were found to be significantly different for $R > 3.5$ and $R < 3.5$. They suggest that low-level jet forcing does not appreciably influence the shear-layer response when strong modes are present; low-level forcing has significant influence when strong modes are absent.

It is readily seen from experimental flow visualization that square wave pulsing of the jet produces discrete vortex rings. This behaviour may be anticipated, since pulsing would produce starting vortices. The main idea proposed in this paper is that the effect of pulsing on jets in crossflow can be explained by considering the behaviour of vortex rings in crossflow. We build on past work by Sau & Mahesh who considered vortex rings in quiescent flow (2007) and a uniform crossflow (2008), respectively. Sau & Mahesh (2007) use direct numerical simulation (DNS) to study

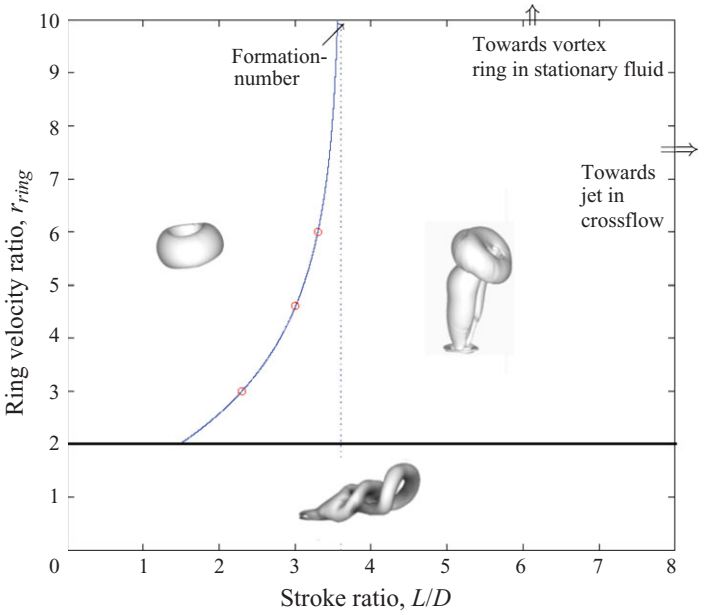

FIGURE 1. (Colour online) Regime map showing three different flow structures of vortex rings in crossflow (Sau & Mahesh 2008).

optimal mixing by a single vortex ring in stationary fluid. They consider two Schmidt numbers and a range of stroke ratios. The formation number is found to yield the maximum entrainment for both Schmidt numbers. Subsequently, Sau & Mahesh (2008) use DNS to study the effect of crossflow on vortex rings. Three different regimes are found to exist depending on the stroke ratio (ratio of stroke length to nozzle exit diameter) and ring velocity ratio (ratio of average nozzle exit velocity to free stream crossflow velocity). A regime map was obtained (figure 1) which categorizes these three different regimes. For velocity ratio less than approximately 2, vortex rings do not form. Instead, a hairpin vortex is obtained at these low velocity ratios. For large stroke ratios and velocity ratios below 2, a periodic train of hairpin vortices is shed downstream. For velocity ratios above 2, two regimes are obtained depending upon stroke ratio. Lower stroke ratios yield a vortex ring tilted upstream, while higher stroke ratios yield a downstream tilted vortex ring accompanied by a trailing column of vorticity. A transition curve in the map defines the transition from a discrete vortex ring to a vortex ring with trailing column. The transition curve is obtained by fitting a curve, which passes through a set of transition stroke ratios obtained from simulations at different ring velocity ratios and has an asymptote at $L/D = 3.6$ (formation number). The transition stroke ratio decreases with decreasing velocity ratio. For very high values of velocity ratio, the transition stroke ratio approaches the 'formation number'.

In this paper, we perform DNS of pulsed jets in crossflow for several jet velocity ratios and pulse conditions. We show that jet penetration and spread can be maximized for specific pulse conditions. We transform the pulsing conditions of the jet into equivalent vortex ring parameters (stroke ratio and velocity ratio), which are then plotted on the regime map (figure 1). The optimal conditions are seen to collapse onto a curve in the regime map. Data from several experiments are then considered, the properties of the resulting vortex rings extracted and the experimental optimal

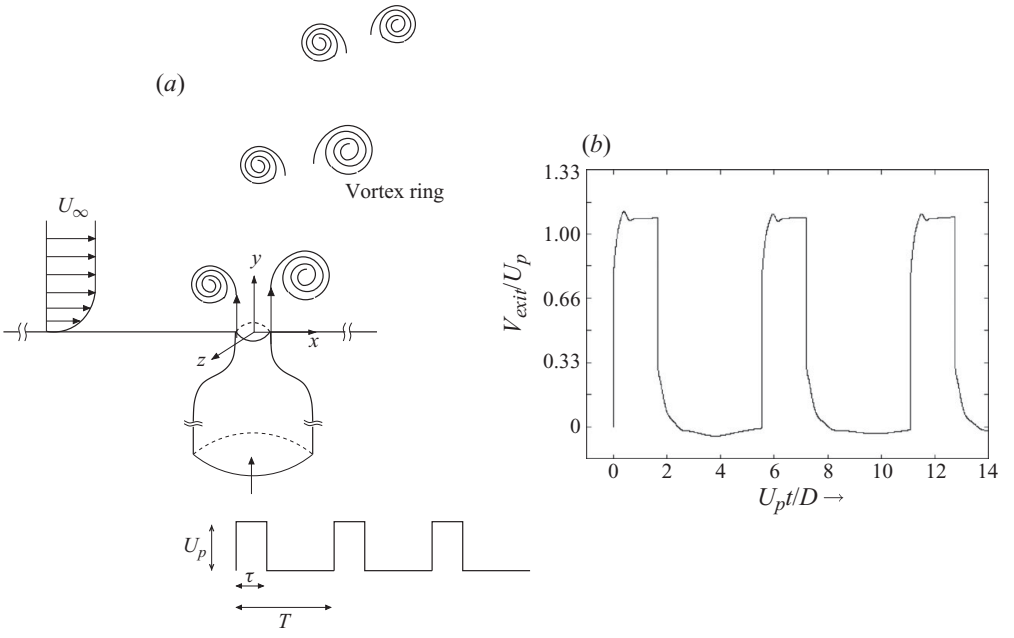

FIGURE 2. (*a*) A schematic of the problem. (*b*) Typical waveform at the nozzle exit resulting from a square waveform specified at the nozzle inflow.

conditions are also seen to collapse onto the same optimal curve in the regime map. This paper is organized as follows. Section 2 discusses the problem, provides details of the simulations and defines the relevant parameters. Simulation results for high velocity ratio pulsed jets in crossflow are presented in § 3. In § 3.3, the simulation results are interpreted in terms of the vortex ring regime map. Experimental results are analysed in § 4. Simulations of very low velocity ratio pulsed jets dominated by hairpin vortices are discussed in § 5. The paper concludes with a brief summary in § 6.

2. Simulation details

2.1. *Problem statement*

A fully modulated pulsed jet is injected through a cylindrical nozzle with 3:1 diameter ratio (figure 2*a*). The nozzle shape of 3:1 diameter ratio is created using an interpolated B-spline curve. In the symmetry plane, the curve is interpolated using the following points: (−0.5, 0, 0), (−0.866, −1, 0) and (−1.732, −1.5, 0). The origin of the coordinate system is located at the centre of the nozzle exit plane, the nozzle axis points in the y-direction and the crossflow is along the x-direction. Pulsing causes the nozzle fluid to form a series of vortex rings as it exits the nozzle. These vortex rings interact with the crossflow, which is modelled as a laminar boundary layer over a flat plate. A square wave velocity profile is prescribed at the nozzle inflow to simulate a pulsed jet. Figure 2(*b*) shows a typical velocity waveform at the centre of the nozzle exit plane. Note that the exit velocity waveform is very close to the square wave prescribed at the nozzle inflow. In experiments, the exit-velocity waveform can be quite different from the prescribed inflow waveform unless some form of control is applied; e.g. M'Closkey *et al.* (2002) use a linear compensator in their experiments to obtain a square waveform at the nozzle exit.

2.2. *Numerical method*

The numerical scheme solves the incompressible Navier–Stokes and continuity equations

$$\frac{\partial u_i}{\partial t} + \frac{\partial u_i u_j}{\partial x_j} = -\frac{\partial p}{\partial x_i} + \nu \frac{\partial^2 u_i}{\partial x_j x_j}, \quad \frac{\partial u_i}{\partial x_i} = 0 \tag{2.1}$$

on unstructured grids. Here u_i, p and ν denote the velocities, pressure and kinematic viscosity, respectively. The density of the fluid is assumed constant and is absorbed into the pressure. The numerical scheme is described in detail by Mahesh, Constantinescu & Moin (2004). The algorithm stores the Cartesian velocities and the pressure at the centroids of the cells (control volumes), and the face normal velocities are stored independently at the centroids of the faces. The scheme is a predictor–corrector formulation, which emphasizes discrete energy conservation on unstructured grids. This property makes the algorithm robust at high Reynolds numbers without numerical dissipation. The predicted velocities at the control volume centroids are obtained using the viscous and the nonlinear terms of (2.1), which are then used to predict the face normal velocities on the faces. The predicted face normal velocity is projected so that continuity is discretely satisfied. This yields a Poisson equation for pressure, which is solved iteratively using a multigrid approach. The pressure field is used to update the Cartesian control volume velocities. Implicit time stepping is performed using a Crank–Nicholson scheme. The algorithm has been validated for a variety of problems over a range of Reynolds numbers (Mahesh *et al.* 2004).

The passive scalar is computed by solving the advection-diffusion equation

$$\frac{\partial C}{\partial t} + \frac{\partial C u_j}{\partial x_j} = \frac{\nu}{Sc} \frac{\partial^2 C}{\partial x_j x_j}, \tag{2.2}$$

where C is the concentration of the scalar. The fluid emerging from the nozzle exit has a value of $C = 1.0$, and the ambient fluid has $C = 0.0$. The spatial derivatives are computed using a predictor–corrector method (Muppidi & Mahesh 2008). The scalar field is first advanced using a second-order central difference scheme. The predicted scalar field is corrected in regions of scalar overshoot using a first-order upwind scheme. This corrector step ensures that the passive scalar concentration is locally bounded (i.e. $C \in [0, 1]$). Also, the scalar is advanced in time using the second-order Adam–Bashforth scheme at a smaller time step than that used for the velocity field. The velocity field is first advanced in time; it is then interpolated in time when needed for the scalar equation.

2.3. *Computational domain and boundary conditions*

The computational domain spans $40\,D \times 40\,D \times 20\,D$ above the nozzle exit in the x-, y- and z-directions, respectively, and includes a $10\,D$ length of nozzle. The crossflow is simulated as a laminar flow over a flat plate. The velocity field from the self-similar Blasius-boundary-layer solution is specified at the inflow plane of the crossflow, $7\,D$ upstream of the nozzle exit. The velocity field is such that in the absence of nozzle fluid, the crossflow has prescribed $\delta_{50\,\%}$ at the centre of the nozzle exit. On the spanwise boundaries ($z/D = \pm 10$), the velocity field corresponding to laminar crossflow over a flat plate is prescribed. Free stream velocity boundary conditions are specified on the top boundary at $y/D = 20$. At the nozzle inflow plane ($y/D = -10$), spatial profile of the specified velocity is a top hat. A zero-gradient boundary condition is used at the outflow.

2.4. *Problem parameters*

Figure 2 shows a schematic of a square wave pulse. The pulse frequency f may be non-dimensionalized using the mean jet velocity $\overline{U}_j$ (obtained by averaging nozzle exit velocity over the nozzle cross-section in one time period T) and the nozzle exit diameter D. This yields the Strouhal number $St = fD/\bar{U}_j$. Duty cycle α is defined as the ratio of pulse width (τ) to the time period ($\alpha = \tau/T$). Here, pulse width is the length of time for which the pulse is 'on'. For a fully modulated jet, the inflow velocity is set to zero when the pulse is 'off'. The peak pulse velocity and free stream crossflow velocities are denoted by U_p and U_∞, respectively. The mean jet to crossflow velocity ratio r_j is defined as the ratio of mean jet velocity $\overline{U}_j$ to U_∞. The Reynolds number based on U_p and nozzle exit diameter (D) is 650 for all simulations in this paper.

The properties of the vortex ring produced during each pulsing cycle may be related to the pulse parameters as follows. In experiments, vortex rings are generated by ejecting a column (length L) of fluid through a nozzle (diameter D). Vortex ring formation is therefore determined by the stroke ratio, L/D. For a square waveform, the equivalent stroke ratio, L/D can be obtained from pulsing parameters (e.g. St, α) as follows. In each cycle, $L = \Delta U_j \tau = \Delta U_j \alpha T$, where ΔU_j is the peak-to-peak velocity. Hence, the stroke ratio

$$\frac{L}{D} = \frac{(\Delta U_j)\tau}{D} = \frac{(\Delta U_j)\alpha}{fD} = \frac{(\Delta U_j)\alpha}{\overline{U}_j} \times \left(\frac{\overline{U}_j}{fD}\right) = \frac{(\Delta U_j)\alpha}{\overline{U}_j} \times \left(\frac{1}{St}\right). \tag{2.3}$$

In the presence of crossflow, another important parameter is the ring velocity ratio (r_{ring}), which is defined as

$$r_{ring} = \frac{\Delta U_j}{U_\infty}. \tag{2.4}$$

Note that for fully modulated (100 % modulation) pulsed jets, the mean jet velocity, $\overline{U}_j = (1/T)\int_0^T u \, \mathrm{d}t = \Delta U_j \alpha$. This implies that

$$\frac{L}{D} = \frac{1}{St} \text{ for 100 \% modulation,} \tag{2.5}$$

$$\frac{L}{D} = \frac{(\Delta U_j)\alpha}{\overline{U}_j} \times \left(\frac{1}{St}\right) \text{ for partial modulation.} \tag{2.6}$$

Note that the vortex ring parameters (L/D, r_{ring}) depend on the 'deviation of velocity' about the mean velocity. On the other hand, the mean jet velocity ratio depends on the mean jet velocity. This observation allows the vortex ring parameters to be consistently computed regardless of jet mean velocity ratio and modulation. Equations (2.3)–(2.6) show how different control strategies determine different ring properties. Assuming that $\overline{U_j}$ and U_∞ are fixed, if the duty cycle α is fixed and St is varied, then L/D varies while r_{ring} stays constant – the path AB in figure 3. If St is fixed and α is changed, L/D stays fixed and r_{ring} varies (path AC). If both St and r_{ring} vary, then L/D varies along with r_{ring} (e.g. path AD).

For a given jet and crossflow combination ($r_j, \overline{U}_j$), there are two independent parameters – St and ΔU_j. The parameters traverse paths similar to AD (with varying duty cycle) as in figure 3. Simulations are performed for fixed ΔU_j (which results in fixed duty cycle), so that there is only one independent parameter, St. In this case, parameters traverse a fixed path like AB in figure 3.

Vortex ring regime, $r_{ring} > 2$

Case	r_{ring}	α (%)	Modulation (%)	Optimal St^*	Optimal $(L/D)^*$	Uncertainty in $(L/D)^*$ (%)
I	8.0	20	100	0.28	3.5	$\pm$7.1
II	8.0	30	100	0.28	3.5	$\pm$7.1
III	6.0	20	100	0.4	2.5	$\pm$5.0
IV	4.5	15	100	0.5	2.0	$\pm$6.2
V	4.5	20	100	0.5	2.0	$\pm$6.2
VI	3.5	20	100	0.67	1.5	$\pm$8.3
VII	10.0	35	100	0.28	3.5	$\pm$7.1
VIII	4.5	25	75	0.21	2.0	$\pm$6.2

TABLE 1. Simulations performed and corresponding optimal conditions.

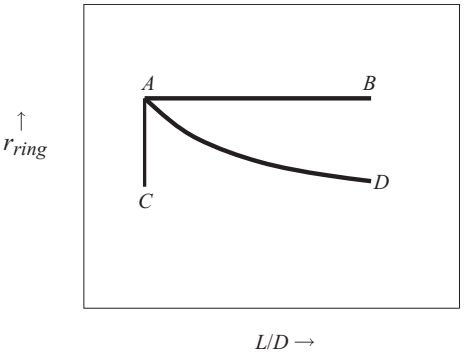

FIGURE 3. Different trajectories in ring parameter space defined in terms of stroke ratio L/D and ring velocity ratio, r_{ring}.

The effect of the oncoming crossflow boundary layer is not studied in this paper.

2.5. *Simulation cases*

Table 1 lists the conditions for the various simulations performed. For different combinations of ring velocity ratio and duty cycle, the stroke ratio L/D (inverse of St) is varied and an optimal stroke ratio is identified. The combination of cases allows the effect of ring velocity ratio and duty cycle on optimal stroke ratio to be assessed. Note that the ring velocity ratio is varied by varying the free stream crossflow velocity. So, for a given ring velocity ratio and duty cycle, mean jet to crossflow velocity ratio (r_j) remains constant as St is being varied. St ranges from 2.0 to 0.167, which corresponds to variation of L/D from 0.5 to 6. Table 1 also tabulates the optimal L/D and corresponding optimal St at different ring velocity ratios and duty cycles. Optimal St corresponds to the frequency which results in the maximum overall penetration for a given jet and crossflow combination. The maximum overall penetration is obtained by the maximum y-location of vorticity or non-zero passive scalar concentration (both yielded the same condition). The optimal condition is obtained by first narrowing down the range where the optimum lies and then performing additional simulations over that range. For example, figure 5 shows simulation results for case II with $L/D = 1.4$, 2.0, 3.5 and 6.0, which correspond to $St = 0.714$, 0.50, 0.28 and 0.167, respectively. However, simulations are also performed

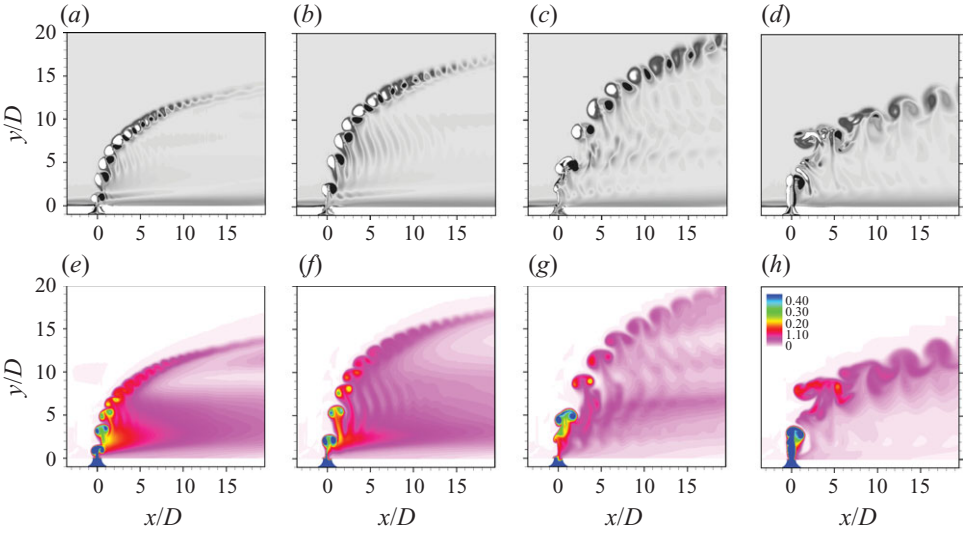

FIGURE 4. (Colour online) Case I: (*a–d*) Contours of z vorticity and (*e–h*) scalar concentration in the symmetry plane. Ring velocity ratio, $r_{ring} = 8.0$, and duty cycle, $\alpha = 20\,\%$, are fixed ($U_p = 3.0$, $U_\infty = 0.38$). Strouhal number is varied: (*a*) and (*e*) $St = 0.714$; (*b*) and (*f*) $St = 0.50$; (*c*) and (*g*) $St = 0.28$; (*d*) and (*h*) $St = 0.167$. Note that maximum penetration is achieved for $St = 0.28$.

for 3.0, 3.25, 3.75 and 4.0. In this case, the uncertainty in the optimal stroke ratio is $\pm 7.1\,\%$. Table 1 lists the uncertainty in optimal stroke ratio for all cases.

3. Simulation results for $r_{ring} > 2$

The behaviour of pulsed jets for $r_{ring} > 2$ is discussed in this section. Optimal pulse conditions at different ring velocity ratios are examined.

3.1. *A 'typical' simulation*

Figure 4 shows the flow field corresponding to case I in table 1. The ring velocity ratio ($r_{ring} = 8$) and duty cycle ($\alpha = 20\,\%$) are fixed while frequency or St is varied: (*a*) $St = 0.714$; (*b*) $St = 0.50$; (*c*) $St = 0.28$; (*d*) $St = 0.167$. Contours of ω_z vorticity (figure 4*a–d*) and the corresponding scalar contours (figure 4*e–h*) in the symmetry plane are shown. Note that the pulsed jet produces a series of discrete vortex rings in each of the cases. In figure 4(*a–c*), upstream tilted vortex rings are produced, and the rings merge and interact further downstream. For $St = 0.167$, in figure 4(*d*), vortex rings with trailing column are produced. These rings strongly interact with their trailing column in the near field. Note that as St decreases from 0.714 (figure 4*a*) to 0.28 (figure 4*c*), the jet penetration increases. Further reduction in frequency results in lower jet penetration as observed in figure 4(*d*). Thus, there exist optimal pulse conditions which maximize penetration of the jet into the crossflow. The jet penetration is maximum at $St = 0.28$ as shown in figure 4(*c*).

In order to quantify mixing, the total volume of scalar-carrying fluid is computed. Schmidt number (Sc) of the scalar is 1. Total volume of scalar-carrying fluid is computed as the sum of all volume elements which have scalar concentrations above a threshold value (set to 0.01) in the domain above the nozzle exit plane ($y/D > 0$). Figure 5 shows the time evolution of total scalar-carrying fluid for different St. After

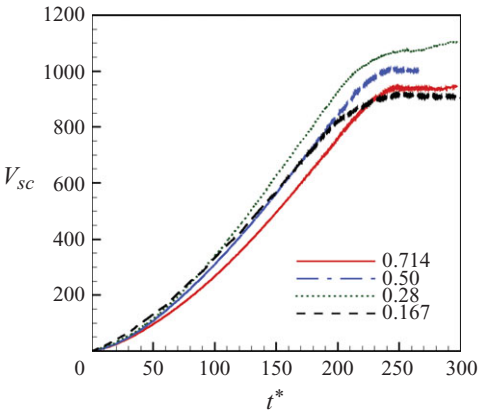

FIGURE 5. (Colour online) Variation of total volume of scalar-carrying fluid with time. Ring velocity ratio is 8.0, duty cycle is 20 %, and several stroke ratios are considered.

the jet exits the domain, the volume of scalar-carrying fluid remains nearly constant. Note that optimal conditions extracted from the total volume of scalar are consistent with those obtained from maximum penetration. The total volume of scalar is also maximum at $St = 0.28$. The passive scalar contours (figure 4*e–h*) reveal an interesting structural feature of pulsed jets in crossflow. Note that (figure 4*e–g*) the jet splits in two streams for $St \geqslant 0.28$. For lower St (e.g. 0.167), no such splitting is observed and only a single stream of the jet is observed (figure 6*h*). In the case of splitting, the second stream is formed by the 'wake of the rings' being convected by the crossflow. At lower St, the rings merge in the near field and the second stream is not pronounced. Fully modulated pulsed jets in crossflow experiments of Eroglu & Breidenthal (2001) reveal similar structural properties and dependence on St. As shown in the simulation, the location of the ring merging moves upstream as St increases. Similar behaviour is observed in the experiments. For very high St (e.g. $St > 2$), the pulsed jet behaves similarly to a regular jet, since the stroke ratio is too small to produce deeply penetrating rings.

3.2. *Effect of velocity ratio and duty cycle*

Figure 6 shows simulation results for case II. Here, conditions are similar to case I except the duty cycle is 30 % instead of 20 %. Figure 6(*a–d*) shows contours of ω_z vorticity and figure 6(*e–h*) shows the corresponding scalar contours in the symmetry plane. Note that the rings interact earlier when the duty cycle is 30 %. However, the overall behaviour is similar to that at the lower duty cycle (20 %). Also, note that varying the duty cycle does not change the optimal Strouhal number. However, for very large duty cycle, e.g. $\alpha > 50$ %, there is no optimal pulsing frequency, since the rings interact in the very near field irrespective of pulsing frequency. The trajectories at very high duty cycle ($\alpha > 50$ %) are similar to that of a regular transverse jet. This behaviour is pronounced at lower ring velocity ratios (3.0–5.0) as discussed later.

The optimal forcing conditions are affected by the ring velocity ratio. Figure 7 shows results for case V in table 1. The ring velocity ratio is lower (4.5) than the preceding cases discussed and the duty cycle is 20 %. Figure 7(*a–e*) shows contours of vorticity in the symmetry plane at different Strouhal number: (*a*) $St = 1.0$; (*b*) $St = 0.5$; (*c*) $St = 0.4$; (*d*) $St = 0.333$; (*e*) $St = 0.2$. Figure 7(*f–j*) shows the corresponding scalar contours in the symmetry plane. Note that the jet penetration varies with the pulsing frequency and maximum penetration is obtained at $St = 0.5$ (figure 7*b*). This optimal

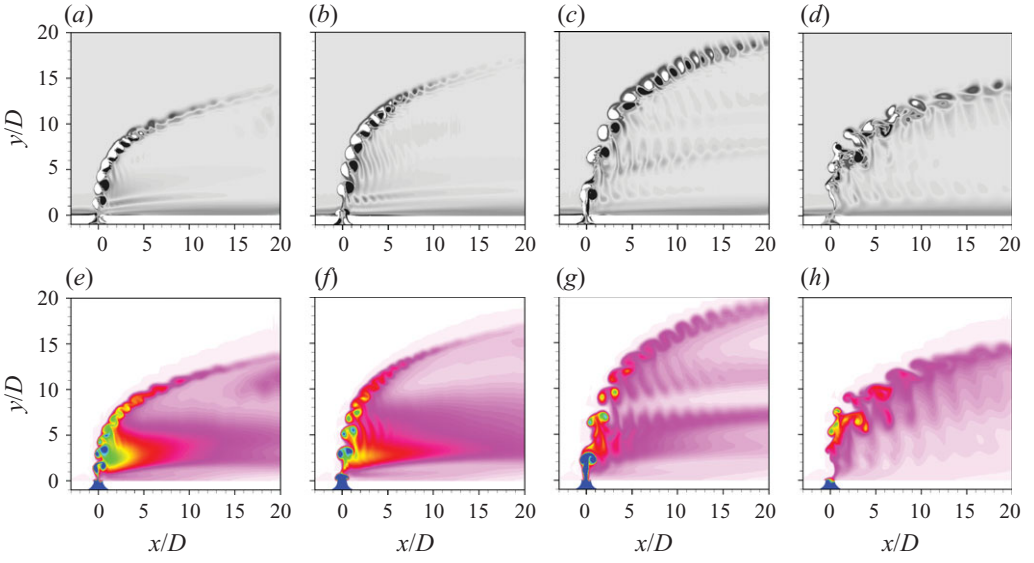

FIGURE 6. (Colour online) Case II: (*a–d*) Contours of z vorticity in the symmetry plane. Ring velocity ratio, $r_{ring} = 8.0$, and duty cycle, $\alpha = 30\,\%$, are fixed ($U_p = 3.0$, $U_\infty = 0.38$). Strouhal number is varied: (*a*) and (*e*) $St = 0.714$; (*b*) and (*f*) $St = 0.50$; (*c*) and (*g*) $St = 0.28$; (*d*) and (*h*) $St = 0.167$. Note that maximum penetration is achieved for $St = 0.28$.

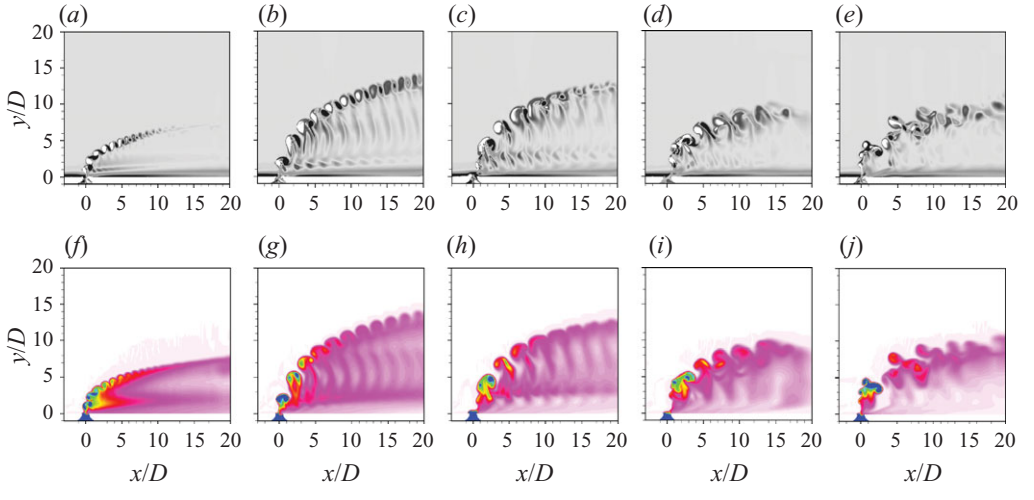

FIGURE 7. (Colour online) Case V: (*a–e*) Contours of z vorticity and (*f–j*) scalar concentration in the symmetry plane. Ring velocity ratio, $r_{ring} = 4.5$, and duty cycle is 20 % ($U_p = 3.0$, $U_\infty = 0.67$). Strouhal number is varied: (*a*) and (*f*) $St = 1.0$; (*b*) and (*g*) $St = 0.5$; (*c*) and (*h*) $St = 0.4$; (*d*) and (*i*) $St = 0.333$; (*e*) and (*j*) $St = 0.2$. Note that the optimal penetration is obtained at $St = 0.5$.

value is higher than the optimal St obtained at $r_{ring} = 8.0$. Also, note that the jet splits into two streams near the optimal pulsing frequency. The ring interactions are much stronger at these low velocity ratios (such as 4.5) and also the trajectories are lower than for the ring velocity ratio of 8.0 (cases I and II).

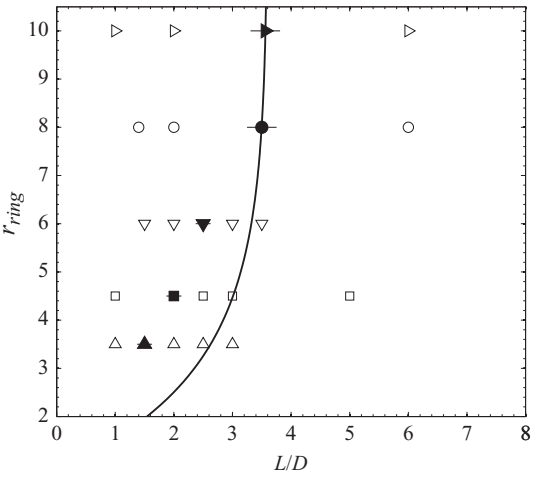

FIGURE 8. Simulation conditions are plotted in stroke ratio and ring velocity ratio coordinates. Note that ○, cases I and II; ∇, case III; □, cases IV and V; △, case VI; ▷, case VII. The filled symbols denote the optimal stroke ratio (table 1) at the corresponding ring velocity ratios. The solid curved line denotes the transition curve for a single vortex ring in crossflow. The horizontal bars around the optimal stroke ratios denote the uncertainty in each case.

The effect of duty cycle at $r_{ring} = 4.5$ was studied by performing simulations at varying duty cycle. For example, at 15 % duty cycle (case IV), the same optimal St is obtained. As observed for $r_{ring} = 8$, the optimal forcing does not change when the duty cycle is lowered. As long as the duty cycle is low enough (but non-zero), e.g. $10\,\% < \alpha < 40\,\%$, optimal forcing conditions are found to exist, and varying the duty cycle only changes penetration difference between optimal and non-optimal cases. For very large duty cycle ($\alpha > 50\,\%$), the ring interactions occur in the very near field at these low velocity ratios (3.0–5.0) and the trajectories resemble that of a regular jet in crossflow. Simulations were also performed at $r_{ring} = 6$ (case III) and 3.5 (case VI) as listed in table 1. For both velocity ratios, optimal pulse conditions are obtained.

3.3. *Interpretation in terms of regime map*

The preceding section showed that an optimal pulsing frequency exists, when pulsing the jet at fixed ring velocity ratio and duty cycle. These optimal conditions may be interpreted in terms of the regime map (figure 1) for single vortex rings in crossflow (Sau & Mahesh 2008). As discussed in § 2.4, the pulsing parameters can be transformed into ring parameters. Recall that a square waveform with 100 % modulation yields an equivalent stroke ratio L/D, which is the inverse of St. Also recall that if the mean jet to crossflow ratio ($r_j = \overline{U}_j / U_\infty$ and $\overline{U}_j = \Delta U_j \alpha$) is fixed, the product of ring velocity ratio (r_{ring}) and duty cycle (α) is fixed. In each of the cases listed in table 1, the time period of the pulse is varied while keeping the pulse velocity fixed. Fixing the pulse velocity (ΔU_j) yields fixed ring velocity ratio (since U_∞ is fixed) and therefore fixed duty cycle. Varying the time period results in variation in stroke ratio. Thus, the pulsing conditions can be transformed into ring parameters and the flow field can be interpreted in terms of the behaviour of vortex rings in crossflow.

Consider case I, which was discussed earlier in figure 4. Here, $r_{ring} = 8.0$ and the equivalent stroke ratios are: (a) 1.4; (b) 2.0; (c) 3.5; (d) 6.0. These conditions are plotted as circles in the regime map in figure 8. The solid circle corresponds to the optimal stroke ratio, $L/D = 3.5$. Note that for stroke ratio less than the transition

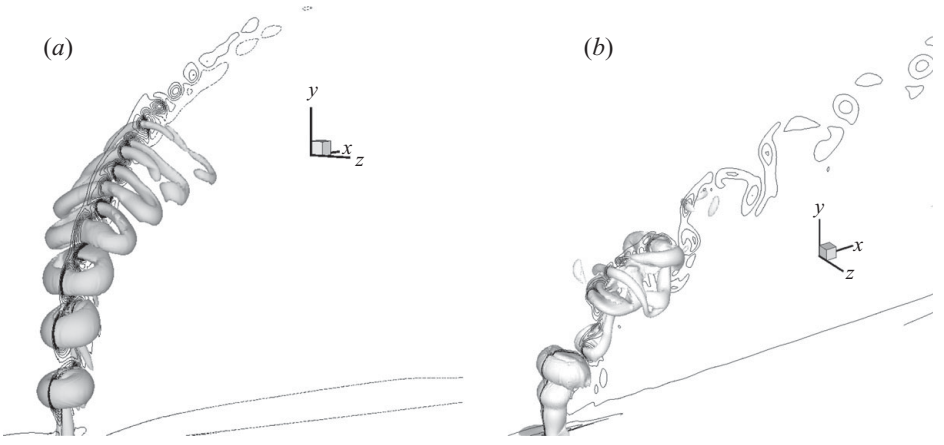

FIGURE 9. (*a*) Ring interactions. (*b*) Ring–column interactions.

stroke ratio ($L/D \leqslant 3.5$ or $St \geqslant 0.28$) in figure 4(*a–c*), the pulsed jet produces a series of upstream tilted vortex rings without any trailing column of vorticity. Vortex rings with $L/D = 1.4$ and 2.0 (figures 4*a* and 4*b*, respectively) contain far less circulation than rings with $L/D = 3.5$ (figure 4*c*). The weaker rings interact in the near field and the penetration is less. In figure 4(*c*), the upstream tilted vortex rings contain maximum momentum when L/D approaches the transition stroke ratio and therefore penetrate deep into the crossflow before interacting with each other. On the other hand, vortex rings with a trailing column of vorticity are produced when the stroke ratio, $L/D = 6$, is higher than the transition stroke ratio (figure 4*d*, $St = 0.167$). These rings have approximately the same momentum as for $L/D = 3.5$ (figure 4*c*), but the trailing columns strongly interact with subsequent ring–column structures in the near field itself. This interaction prevents deep penetration into the crossflow. Optimal penetration is therefore obtained at $St = 0.28$ or $L/D = 3.5$ for $r_{ring} = 8$. Simulations are also performed at $r_{ring} = 10$ (case VII). The results are similar to $r_{ring} = 8$. The optimal condition corresponds to $St = 0.28$ or $L/D = 3.5$ (figure 8).

Next, consider simulations at $r_{ring} = 4.5$ (case V, figure 7). The equivalent stroke ratios vary from 1.0 (figure 7*a*) to 5.0 (figure 7*b*). The equivalent vortex ring parameters are plotted using square symbols on the regime map in figure 8. The solid square symbol represents the optimal stroke ratio. Note that the optimum lies left of the transition curve unlike its behaviour at the higher velocity ratio discussed above. The same behaviour is observed for simulations performed at $r_{ring} = 6$ (case III) and 3.5 (case VI) listed in table 1. These two cases are marked by triangles in figure 8. A curve representing optimal stroke ratios at different velocity ratios can be estimated passing through the points shown in the figure. Note that this curve coincides with the transition curve at higher velocity ratios and falls to the left of the transition curve at lower ring velocity ratios. The optimal stroke ratio decreases as the ring velocity ratio decreases. Recall that the transition curve represents the transition in structure and tilting for a 'single' vortex ring in crossflow. The reason for the shift of optimal condition from the transition curve is due to the interaction between successive rings. At low ring velocity ratios, the interaction between successive rings increases as the stroke ratio increases. This mutual interaction is stronger at lower ring velocity ratios.

3.4. *Ring interactions*

The interaction between successive rings is qualitatively different for the regimes that produce upstream-tilting vortex rings and downstream-tilting rings with trailing

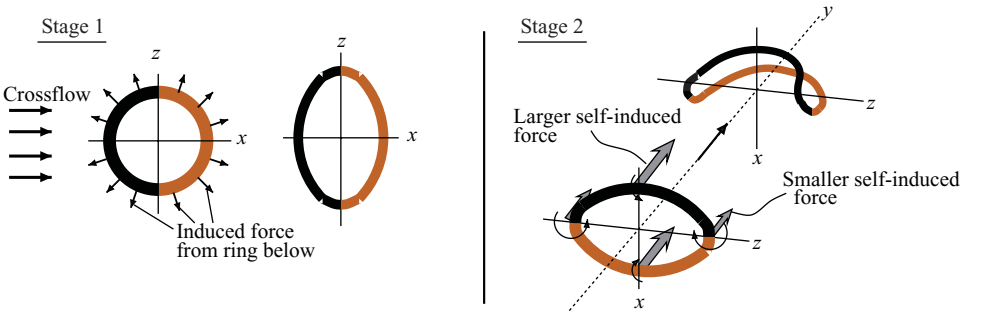

FIGURE 10. (Colour online) Schematic to explain ring deformation.

column. In the absence of a trailing column, ring–ring interactions (figure 9*a*) cause out-of-plane stretching and deformation of the rings. Note that as the rings evolve, they stretch in the spanwise direction and deform out-of-plane to develop a 'bow-like' shape. Also, filaments with opposite spanwise vorticity come closer in the streamwise direction. The evolution and deformation of these rings can be explained using self- and mutual induction (figure 10).

When a single vortex ring exits the nozzle, it tilts upstream as explained in Sau & Mahesh (2008). The subsequent ring will induce a force to expand the upper ring radially outward similar to the leapfrog mechanism of two vortex rings. However, the interaction between the streamwise crossflow and the ring leads to a straining flow in the plane of the ring. The straining flow stretches the ring in the spanwise direction (stage 1, figure 10). The ring evolves into a tilted elliptic ring. Marshall & Grant (1994) studied the effect of straining flow on the evolution of vortex rings using linear theory and the vortex element method. They suggest that depending on the degree of straining, either the ring alternately elongates in the direction of the stretching and compression of the external flow or the ring monotonically elongates in the direction of the stretching of the external flow without oscillation. In the present simulations, the latter scenario is observed. An elliptic ring has smaller distance between streamwise filaments; this yields larger self-induced force on the streamwise filaments and the ring deforms into a 'bow-like' shape in later stages (figure 10, stage 2). When a trailing column is present, (figure 9*b*), the ring above the column expands and reduces in speed while the trailing column enters into the ring structure. Even at moderate duty cycle, the trailing column strongly interacts with the ring below it.

3.5. *Partially modulated pulsed jets*

All simulations discussed thus far, consider pulsed jets with 100 % modulation; i.e. the minimum jet velocity during a time period is zero. Note that percentage modulation is defined as the ratio of the peak-to-peak jet velocity to maximum jet velocity. The optimal values in figure 8 correspond to simulation cases with 100 % modulation. For partially modulated jets the peak-to-peak velocity difference is fixed and the lower bound of the prescribed jet velocity is non-zero. The equivalent stroke ratio and ring velocity ratio should be based on the peak-to-peak velocity difference and crossflow free stream velocity as defined in § 2. When defined in this manner, the optimal combination of stroke and ring velocity ratios in a partially modulated jet is the same as fully modulated jet (figure 8).

An additional set of simulations were performed for a 75 % modulated jet with ring velocity ratio of 4.5 as shown in figure 11. Contours of z vorticity (figure 11*a–c*) and scalar concentration (figure 11*d–f*) are plotted in the symmetry plane. The Strouhal

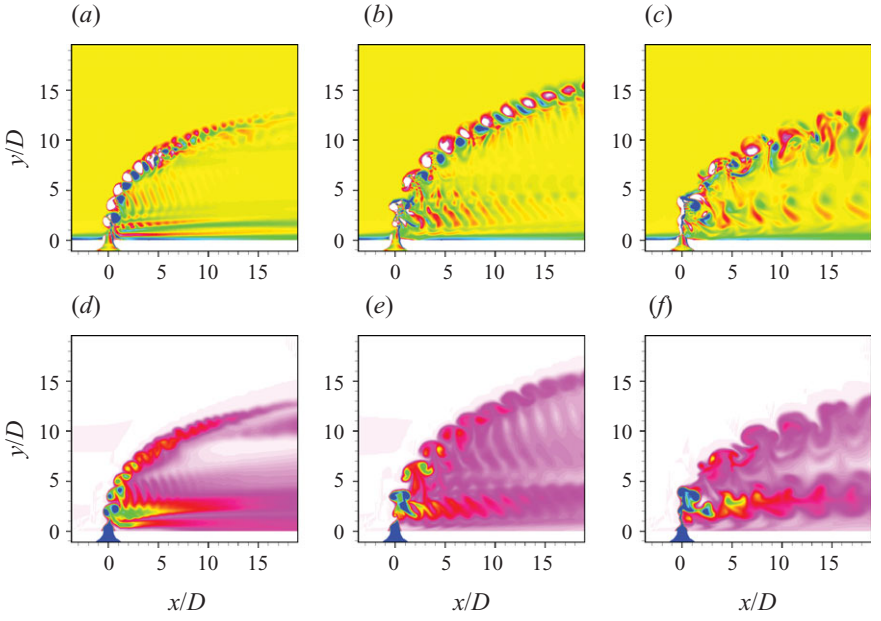

FIGURE 11. (Colour online) The effect of partial modulation (75 %). (*a–c*) Contours of z vorticity and (*d–f*) scalar concentration in the symmetry plane. Ring velocity ratio, $r_{ring} = 4.5$ and duty cycle is 25 % ($\overline{U}_j = 1.75$, $\Delta U = 3.0$, $U_\infty = 0.67$). Strouhal number or Stroke ratio is varied: (*a*) and (*d*) $St = 0.43$, $L/D = 1.0$; (*b*) and (*e*) $St = 0.21$, $L/D = 2.0$; (*c*) and (*f*) $St = 0.11$, $L/D = 4$. Note that optimal penetration is obtained at $St = 0.21$ or equivalent stroke ratio of 2 and $r_{ring} = 4.5$.

number St is varied ($St =$ (*a*) 0.43, (*b*) 0.21 and (*c*) 0.11) while keeping the duty cycle ($\alpha = 25\,\%$) and ring velocity ratio ($r_{ring} = 4.5$) constant. As discussed in § 2, $St = D/L$ for 100 % modulation. On the other hand, for partial modulation, the relation will involve the base flow. In this particular case, $St = 0.43 \times D/L$. Figure 11(*b*) shows that optimal penetration corresponds to equivalent stroke ratio of 2. Recall that the optimal stroke ratio was 2 at ring velocity ratio of 4.5 for a fully modulated jet. Thus, optimal conditions can be predicted even for partial modulation using the equivalent stroke ratio and ring velocity ratio as shown in figure 8.

Note that in all the cases in figure 11(*d–f*), the scalar contours show multiple streams for the pulsed jet. Even in the regime where the vortex ring has a trailing column (e.g. figure 11*f*, $L/D = 4$), the jet splits in two streams unlike the fully modulated jet. This is because the minimum jet velocity is non-zero for partially modulated jets. So, the jet basically consists of high-momentum fluid that generates rings and low-momentum fluid that stays close to the wall. The second stream is mainly jet fluid with non-zero jet velocity during the period when the pulse is 'off'.

3.6. *Effect of 'experimental square' waveform*

The simulations in this paper are performed using square wave excitation at the nozzle inflow. The corresponding waveform obtained at the nozzle exit is very close to a square waveform, as discussed in § 2. However, exit waveforms in experiments are not perfect square waves. The effect of this deviation from a perfect square waveform is therefore investigated. A simulation is performed with a modified square waveform corresponding to the experiments of Shapiro *et. al* (2006). Figure 12(*a*) shows the

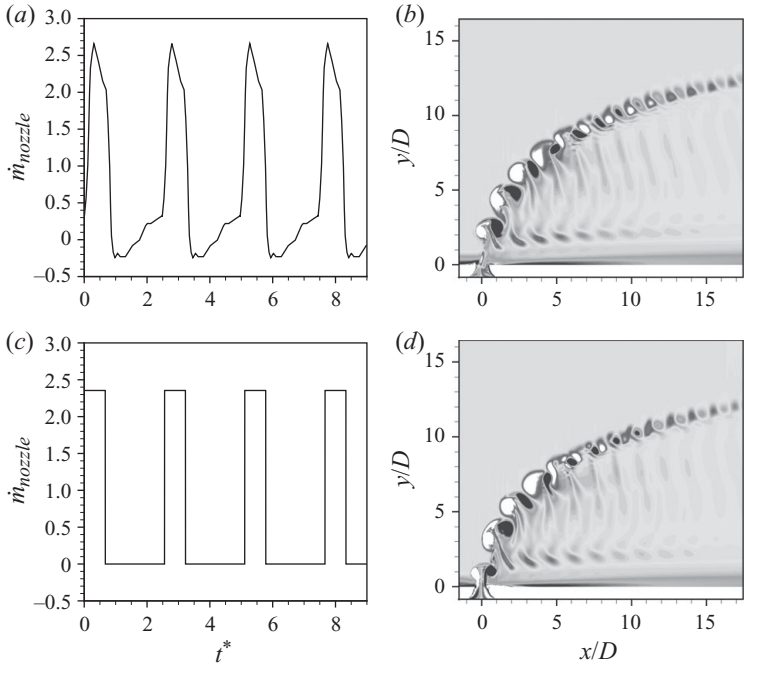

FIGURE 12. (*a*) and (*b*) Mass flow rate at the nozzle exit and corresponding flow field for a waveform similar to the experiments of Shapiro *et al.* (2006). (*c*) and (*d*) Mass flow rate at the nozzle exit and corresponding flow field for a square waveform. Both waveforms have the same stroke ratio, velocity ratio and duty cycle.

waveform from one of their experiments (figure 3*b*, page 1295 of their paper). The modified square waveform (figure 12*a*) is scaled to yield a stroke ratio of 2 and ring velocity ratio of 4.5. The duty cycle of the waveform is 27 %. The equivalent square waveform is shown in figure 12(*c*). Figure 12(*b*, *d*) shows spanwise vorticity contours in the symmetry plane for both waveforms. Note that there is hardly any difference in either trajectory or the vorticity field. This is because the flow depends largely on the amount of circulation imparted during the pulse (stroke ratio) and velocity ratio. The circulation is not significantly affected by the deviations from a perfect square waveform in the experiments. The flow fields will therefore be consistent as long as the stroke ratio and velocity ratios are properly computed.

4. Interpretation of and comparison to experimental results

In this section, we consider results from several experiments and interpret the optimal conditions in terms of the regime map. We show that the optimal conditions in experiments can be predicted/explained using the stroke and ring velocity ratios of the equivalent vortex rings. Also, while the optimal *St* or duty cycles vary over a wide range, the regime map shows good collapse of optimal conditions between the various experiments and the simulations discussed earlier.

4.1. *Experiment of Shapiro et al. (2006)*

Shapiro *et al.* (2006) performed controlled experiments of pulsed jets in crossflow. They note that specific combinations of pulse widths and forcing frequencies produce deeply penetrating vortex rings and bifurcating jets, and that the jet penetration is

Case	$\bar{U}_j$ (m s^{-1})	U_∞	r_j	$U'_{j,rms}$	Re_j	f (Hz)	α or τ (%)	τ_{opt} (ms)
1	2.8	1.1	2.58	1.5	1420	44–147	10–50	3.0
4	7.2	1.8	4.0	2.3	3660	87–130	10–50	1.6

TABLE 2. Experimental conditions of Shapiro *et al.* (2006).

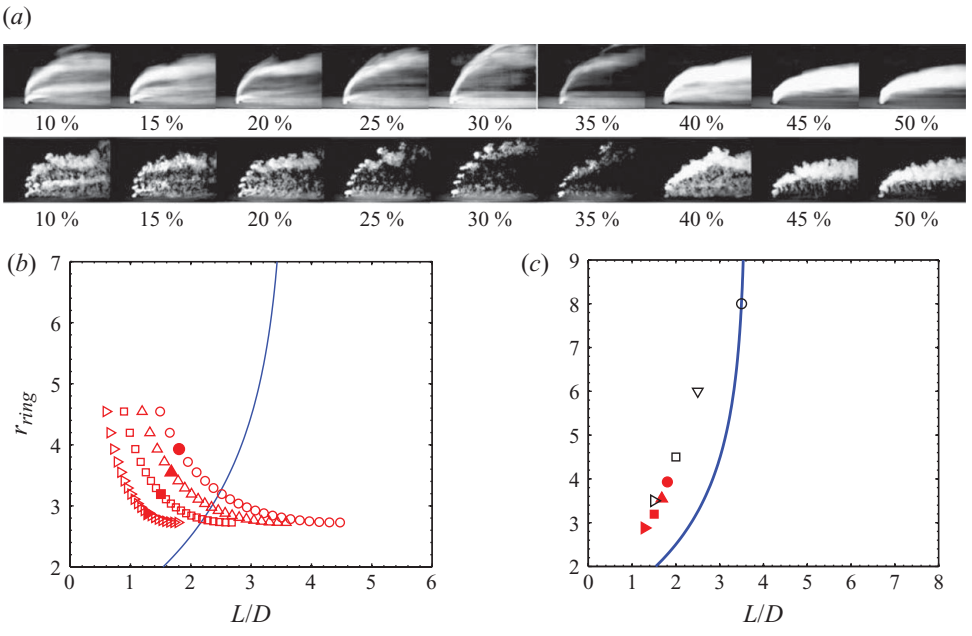

FIGURE 13. (Colour online) (*a*) Figure 4 from experiment of Shapiro *et al.* (2006), reprinted by permission; mean and instantaneous flow field (case 1, $U'_{j,rms} = 1.5\,\mathrm{m\,s^{-1}}$) with forcing frequency $f = 110$ Hz for duty cycle ranging from 10–50 %. Maximum jet penetration occurs at 30 % duty cycle and corresponds to optimal pulse width ($\tau = 3$ ms). (*b*) The experimental conditions for varying pulse width or duty cycle are transformed in regime map for four frequencies: ○, 44 Hz; △, 55 Hz; □, 73.5 Hz; ▷, 110 Hz. Filled symbols show the optimal conditions ($\tau = 3$ ms) at corresponding frequencies. The solid line denotes the transition curve. (*c*) Optimal conditions from experiments are compared to simulations. Filled and open symbols correspond to experiment and simulations, respectively.

maximum under these conditions. Their experiments considered four different jet and crossflow combinations at two different mean jet to crossflow velocity ratios, 2.58 and 4.0. Table 2 lists experimental conditions for two cases denoted by 1 and 4 in their paper with jet velocity ratios 2.58 and 4.0, respectively. For each case, the frequency is fixed and the pulse width is varied such that $U'_{j,rms}$ is constant (table 2). Since frequency is fixed and duty cycle is varied such that $U'_{j,rms}$ is constant, both stroke ratio L/D and ring velocity ratio r_{ring} vary. As the duty cycle increases, L/D increases and r_{ring} decreases. For each experiment of Shapiro *et al.* (2006), the parameters can be transformed into ring parameters and interpreted accordingly.

Figure 13 considers case 1 (table 2) of Shapiro *et al.* (2006). Figure 13(*a*) reproduces from their paper the mean and instantaneous flow field at 110 Hz when the duty cycle varies from 10–50 %. Optimal penetration is obtained at duty cycle of 30 % with pulse width of 3 ms. The optimal pulse widths at the other frequencies (44, 55, 73.5 Hz) are

Frequency (Hz)	r_j	Optimal τ (ms)	Optimal ring parameters	
			L/D^*	r_{ring}
44	2.58	3	1.80	3.93
55	2.58	3	1.68	3.55
73.5	2.58	3	1.50	3.19
110	2.58	3	1.28	2.88

TABLE 3. Case 1 of Shapiro *et al.*; optimal conditions ($U'_{j,rms}$ is matched at 1.5 m s^{-1}).

Frequency (Hz)	r_j	Optimal τ (ms)	Optimal ring parameters	
			L/D^*	r_{ring}
87	4.0	1.6	1.40	3.68
96.7	4.0	1.6	1.34	3.53
124.3	4.0	1.6	1.21	3.19

TABLE 4. Case 4 of Shapiro *et al.*; optimal conditions ($U'_{j,rms}$ is matched at 2.3 m s^{-1}).

also reported to have the same value of 3 ms. Figure 13(*b*) shows the corresponding vortex ring parameters for the four different frequencies (44, 55, 73.5 and 110 Hz for case 1) using different symbols. The stroke and ring velocity ratios are computed using the peak-to-peak velocity difference. Note that at a given frequency, as the pulse width increases at fixed $U'_{j,rms} = 1.5\,\mathrm{m\,s^{-1}}$, stroke ratio increases and ring velocity ratio decreases. The optimal pulse width of 3 ms for each of these frequencies is denoted by solid symbols. The optimal stroke ratios and ring velocity ratios are also listed in table 3. Note that the optimal conditions lie on the left of the transition curve and decrease with ring velocity ratio as shown in figure 13(*b*). In figure 13(*c*), these optimal conditions are compared to optimal stroke ratios obtained in simulations. Note that good agreement is obtained and the experimental optimal conditions follow the same trend as the simulations.

The flow structures in figure 13(*a*) are interesting to observe. Below the optimal duty cycle of 30 %, discrete upstream-tilted vortex rings are evident. Note that the rings interact in the near field and the penetration is less at lower pulse width or duty cycle (10–20 %). In these cases, the equivalent stroke ratios are much smaller than their transition values (less than 1) as noted in figure 13(*b*). These rings therefore contain much less circulation, which results in less penetration. Around the optimal duty cycle (25–35 %), upstream-tilted vortex rings are produced that penetrate deep into the crossflow before interacting or merging with each other. At even higher duty cycle (40–50 %), the rings interact in the very near field and the pulsed jet looks more like a steady jet. This behaviour is similar to that observed in the simulations in § 3.

Case 4 in Shapiro *et al.*'s experiments examines optimal pulse width at various frequencies. The experimental conditions for case 4 are listed in table 2. The pulse width is varied at fixed frequency such that $U'_{j,rms} = 2.3\,\mathrm{m\,s^{-1}}$. In this case, the optimal pulse width is found to be 1.6 ms at all the frequencies. Figure 14(*a*) plots the experimental conditions in the regime map for three frequencies (87, 96.7 and 124.3 Hz) as the pulse width is varied. Note that as the pulse width increases, stroke ratio increases and ring velocity ratio decreases. The optimal conditions are listed in table 4 and marked using solid symbols in figure 14(*a*). Figure 14(*b*) compares the optimal experimental conditions to simulation results. Note that good agreement is obtained.

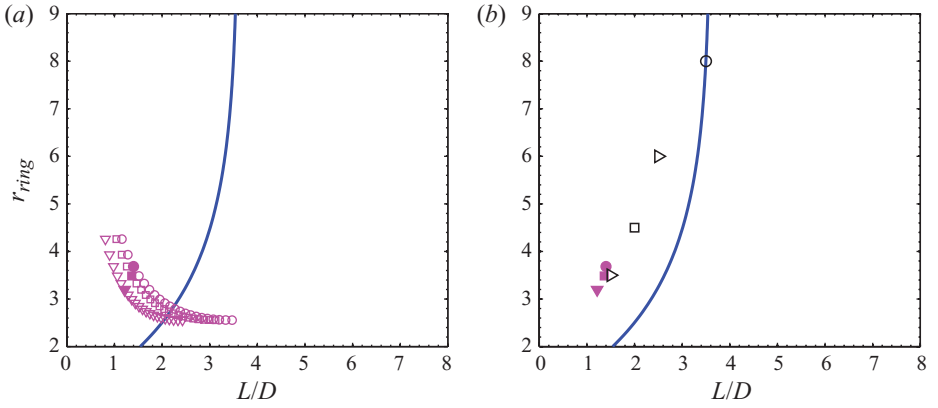

FIGURE 14. (Colour online) (*a*) Experimental conditions (case 4 of Shapiro *et al.*, $U'_{j,rms} = 2.3\,\mathrm{m\,s^{-1}}$) with varying pulse width for different frequencies, ○, 87 Hz; □, 96.7 Hz; ∇, 124.3 Hz, are plotted in stroke ratio and ring velocity ratio space. Filled symbols show the optimal conditions with pulse width 1.6 ms. Solid line denotes the transition curve. (*b*) Optimal condition for the experiment is compared with simulations. Filled and open symbols correspond to experiment and simulations, respectively.

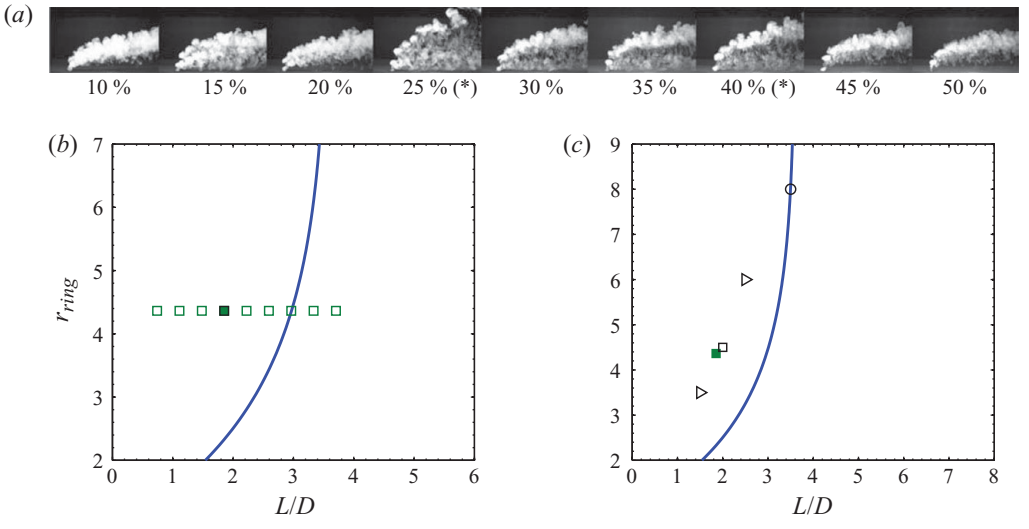

FIGURE 15. (Colour online) (*a*) Figure 6(*c*) from experiment of Shapiro *et al.* (2006), reprinted by permission; smoke visualization for experimental case 1, with peak-to-peak ΔU_j fixed at $4.8\,\mathrm{m\,s^{-1}}$ with forcing frequency $f = 85\,\mathrm{Hz}$ for duty cycle ranging from 10–50 %. Maximum jet penetration occurs at 25 % duty cycle. (*b*) Experimental conditions are plotted in stroke ratio and ring velocity ratio space. Filled symbol shows the optimal condition with duty cycle 25 %. The solid line denotes the transition curve. (*c*) Optimal condition for the experiment is compared to simulations. Filled and open symbols correspond to experiment and simulations, respectively.

Shapiro *et al.* (2006) also perform experiments where they fix the peak-to-peak jet velocity excitation amplitude ΔU_j and frequency, while varying the duty cycle. Note that as the duty cycle increases for fixed ΔU_j, the stroke ratio increases while ring velocity ratio stays fixed. Figure 15(*a*) shows the instantaneous flow field for different duty cycles (10–50 %) at 85 Hz and $\Delta U_j = 4.8\,\mathrm{m\,s^{-1}}$. The experimental conditions for this case are transformed into corresponding vortex ring parameters space in

Frequency (Hz)	r_j	Optimal α (%)	Optimal ring parameters	
			L/D^*	r_{ring}
55	2.58	15	1.718	4.36
73.5	2.58	20	1.714	4.36
85	2.58	25	1.852	4.36

TABLE 5. Case 1 Shapiro *et al.*; optimal condition (ΔU_j is matched at 4.8 m s^{-1}).

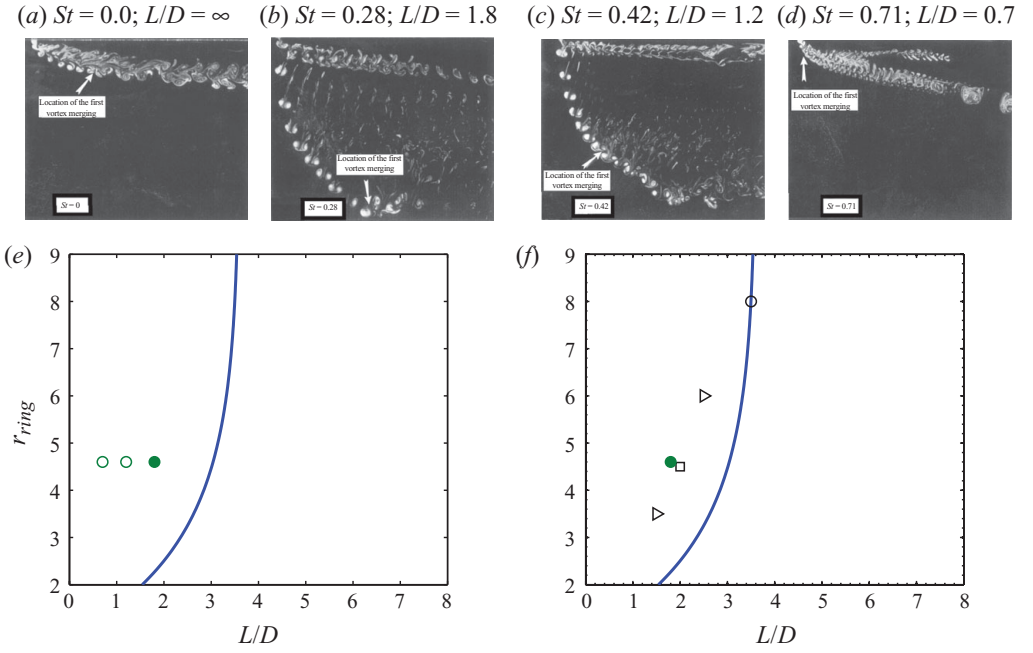

FIGURE 16. (Colour online) Results from the experiments of Eroglu & Breidenthal (2001, reproduced by permission) showing pulsed jets in crossflow at different Strouhal numbers. (*a*) The steady jet, $St = 0.0$. Ring velocity ratio is 4.6 in all cases. The equivalent stroke ratios (L/D) are (*b*) 1.8, (*c*) 1.2 and (*d*) 0.7. Note figure (*b*) shows the maximum penetration for $L/D = 1.8$. (*e*, *f*) Corresponding regime map.

figure 15(*b*). Note that optimal penetration is achieved at duty cycle of 25 %. This optimal duty cycle of 25 % at 85 Hz corresponds to L/D of 1.8 at $r_{ring} = 4.36$ (solid symbol in figure 15*b*). The optimal condition is plotted along with the simulation results in figure 15(*c*). Note that good agreement is obtained. The optimal duty cycles for three different frequencies (55, 73.5 and 85 Hz) and the corresponding ring parameters are listed in table 5.

4.2. *Experiment of Eroglu & Breidenthal (2001)*

Eroglu & Breidenthal (2001) study fully modulated pulsed transverse jets with square wave excitation at 50 % duty cycle. Figure 16(*a–d*) shows the flow field in their experiments at different pulsing frequencies (*a*) $St = 0.0$ (steady jet), (*b*) $St = 0.28$, (*c*) $St = 0.42$ and (*d*) $St = 0.71$. The mean jet to crossflow velocity ratio is fixed at 2.3, which corresponds to a ring velocity ratio of 4.6. The equivalent stroke ratios for these cases are shown in figure 16(*a–d*). It is clear that discrete vortex rings are produced at

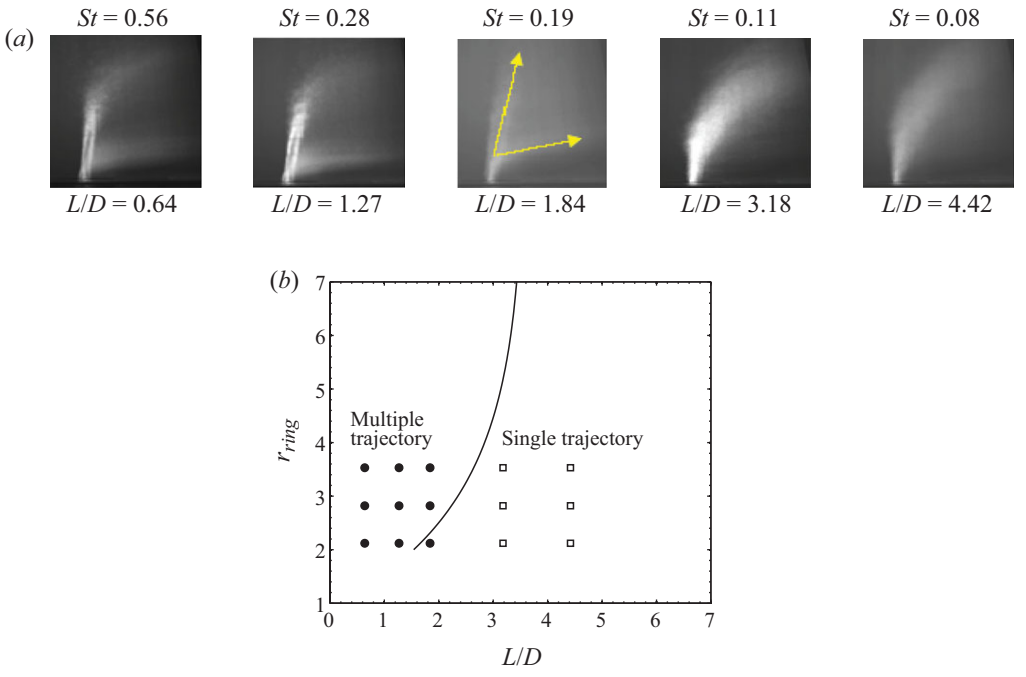

FIGURE 17. (Colour online) (*a*) Experiments of Tomar, Arnaud & Soria (2004, reproduced by permission) on ZNMF–JIC reveal that for $St \geqslant 0.19$ (corresponds to $L/D \leqslant 1.84$), the mean jet structure has multiple trajectories and for $St < 0.11$ ($L/D > 3.18$) the jet has a single trajectory. The equivalent ring velocity ratio for this case corresponds to 3.53. (*b*) Symbols correspond to transformed experimental data in ring parameter space. Filled and open symbols correspond to multiple and single trajectory structure, respectively.

$St = 0.28$, which penetrate the crossflow in the near field and interact/merge further downstream. Also the jet splits in two streams. As the frequency is increased to $St = 0.42$, the location of the first interaction shifts upstream and the jet penetration is lower. Again, as the frequency is increased to $St = 0.71$, the rings interact in the very near field and the penetration is much lower than the other two cases. This behaviour is consistent with that observed in the simulations. The experimental conditions are transformed onto the regime map in figure 16(*e–f*). Note that the stroke ratio for optimal penetration lies very close to the optimal stroke ratios obtained in the simulations.

4.3. *Zero-net-mass-flux jet in crossflow by Tomar et al. (2004)*

Tomar *et al.* (2004) study the effect of Strouhal number and velocity ratio on the mean structure of zero-net-mass-flux jets in crossflow (ZNMF–JIC) using planar laser-induced fluorescence. Experiments are performed for velocity ratios ranging from 2 to 5 and Strouhal numbers varying from 0.08 to 0.56. They observe two distinct flow regimes depending on St as shown in figure 17(*a*). Figure 17(*a*) shows the mean structure of the jet as St is varied at velocity ratio of 5. A single mean jet trajectory is observed for $St < 0.11$ and multiple trajectories are observed for $St > 0.19$. Tomar *et al.* (2004) also suggest that the multiple trajectory ZNMF–JIC penetrates more deeply into the ambient crossflow. Table 6 lists the vortex ring parameters computed for their experiments. The equivalent stroke ratio ranges from 0.64 to 4.42 and the ring velocity ratio varies from 1.41 to 3.16. Ring parameters are computed

St	*L/D*	Mean structure
0.08	4.42	single trajectory
0.11	3.18	single trajectory
0.19	1.84	multiple trajectory
0.28	1.27	multiple trajectory
0.56	0.64	multiple trajectory

TABLE 6. Experiments ZNMF-JIC (Tomar *et al.* 2004).

from maximum piston velocity, orifice diameter and free stream crossflow velocity. Note that for $L/D = 0.64$, 1.27 and 1.84, multiple trajectories are observed while for $L/D = 3.18$ and 4.42, single trajectories are observed. These conditions are plotted on the regime map in figure 17(*b*). The experimentally observed behaviour is consistent with our simulations of fully modulated jets in crossflow. When the pulsing produces single vortex rings without any trailing column, multiple trajectories are observed as shown in figures 6(*g*) and 7(*g*). As observed in their experiments, the multiple trajectory jets penetrate deeper into the crossflow.

5. Simulation results for $r_{ring} < 2$

The behaviour of pulsed transverse jets at low velocity ratios is fundamentally different from that at high velocity ratios. This difference may be traced back to the behaviour of vortex rings in crossflow at low velocity ratios. As discussed by Sau & Mahesh (2008) and summarized in § 1, at low velocity ratios (less than 2), pulsing into a crossflow produces hairpin vortices and not vortex rings. The hairpin vortices form on a certain time scale; if the pulse duration is longer than this time scale, a series of hairpins is shed in a periodic manner. Even a continuous, low velocity ratio jet sheds hairpins. This shedding frequency depends on velocity ratio and Reynolds number. Most of the entrainment of crossflow fluid is due to the hairpin legs.

Here, simulations of continuously pulsed low velocity jets in crossflow are performed. Optimal pulse frequencies are examined at different velocity ratios. Note that for a fixed velocity ratio and duty cycle, varying the frequency changes the length of the pulse (stroke ratio). As discussed above, as long as the pulse length is longer than the time scale on which the hairpins are shed, hairpin structures will form and shed periodically regardless of the pulse Strouhal number *St* or stroke ratio L/D. It is therefore expected that penetration of the pulsed jet will not change when the pulsing frequency is varied. The simulation results confirm this behaviour. Figure 18 shows results for a velocity ratio of 0.75 with constant duty cycle of 75 % at different *St* or L/D. Instantaneous scalar contours are plotted in the symmetry plane and show the cross-sections of the hairpin heads. The mean mass flow rate and scalar injection rate through the nozzle exit are held constant while the frequency is varied. The total volume of scalar-carrying fluid (V_{sc}), after initial transients exit the domain, is computed as a metric for mixing. Figure 19 shows how V_{sc} in the domain varies with time for various stroke ratios at velocity ratio of 0.75 and duty cycle of 75 %. The initial transients exit the domain around $t^* = 35$. For each L/D, V_{sc} remains constant after the flow has exited the domain. This constant value of V_{sc} is compared for different L/D. Note that V_{sc} increases with stroke ratio till $L/D = 2.5$, then remains approximately constant as stroke ratio increases. This behaviour can be explained as follows.

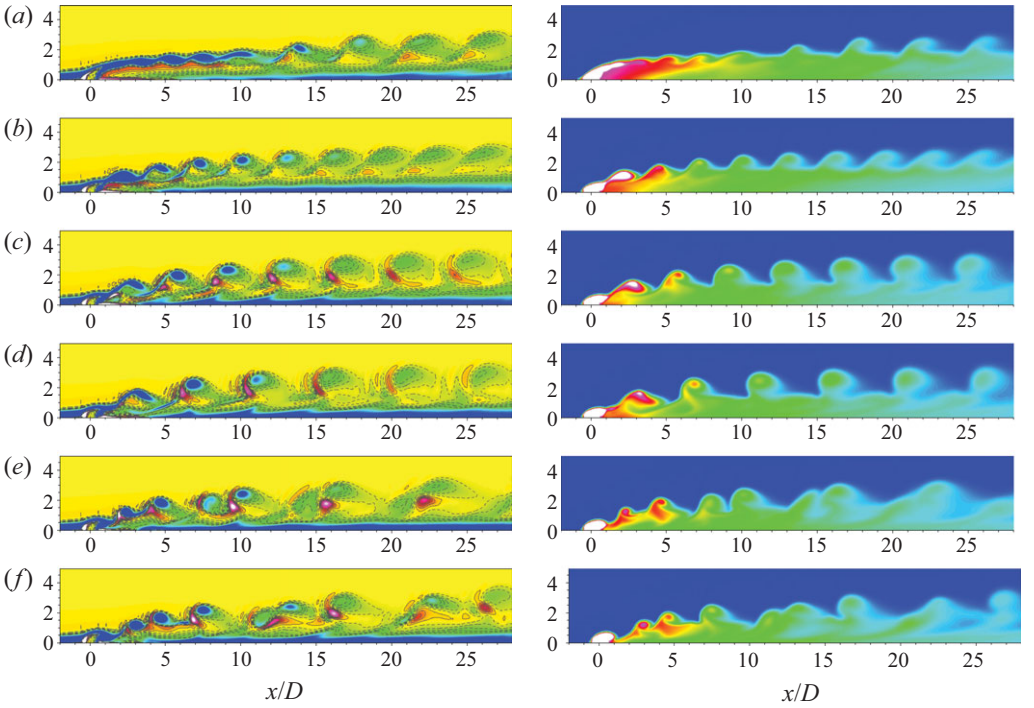

FIGURE 18. (Colour online) Ring velocity ratio = 0.75, duty cycle = 75 %. Contours of vorticity and scalar are plotted in the symmetry plane at different stroke ratios: (*a*) 1.0, (*b*) 2.0, (*c*) 2.5, (*d*) 3.0, (*e*) 4.0 and (*f*) 6.0. (The length scales on the vertical axes are all y/D.)

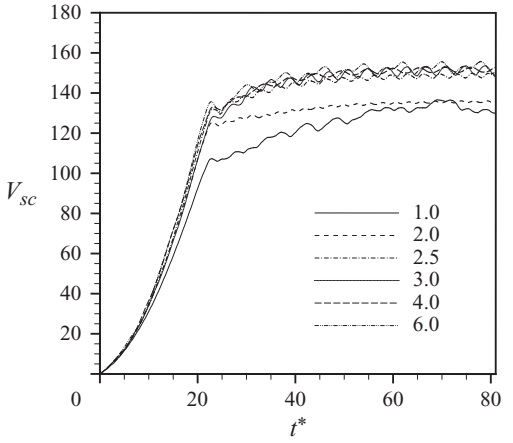

FIGURE 19. Variation of total volume of scalar-carrying fluid in the domain with time. The ring velocity ratio is 0.75, duty cycle is 75 % and different stroke ratios are considered.

5.1. *Timescale of hairpin formation*

As mentioned above, there is a natural time scale on which hairpins form at each velocity ratio and Reynolds number. For lower stroke ratios such as $L/D = 1$ or 2, the pulse width is smaller than the natural time scale of hairpin formation. As a result (figure 18*a*, *b*), the hairpins are much smaller and weaker. The legs of these

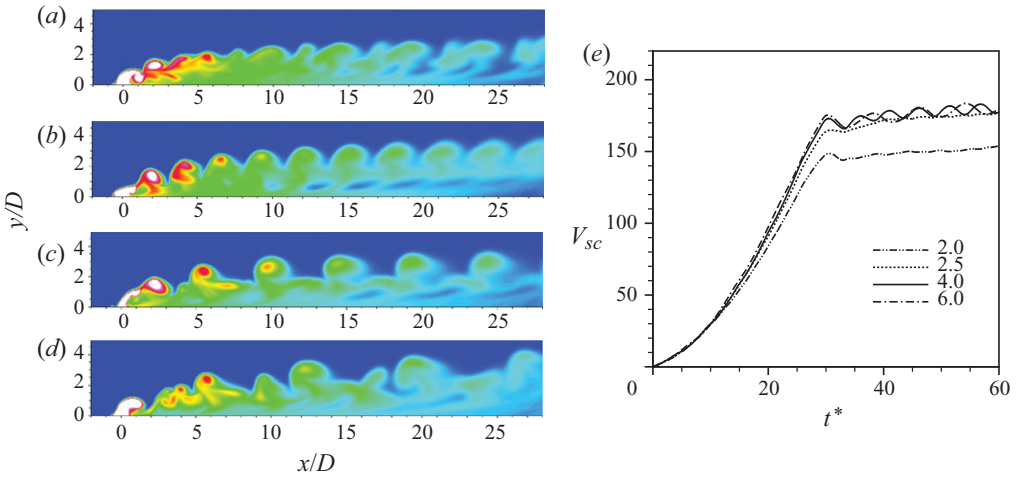

FIGURE 20. (Colour online) Ring velocity ratio = 1.0, duty cycle = 75 %. Contours of scalar in the symmetry plane at different stroke ratios: (*a*) 2.0, (*b*) 2.5, (*c*) 4.0 and (*d*) 6.0. (*e*) Variation of total volume of scalar-carrying fluid in the domain with time. Ring velocity ratio is 1.0, duty cycle is 75 % and different stroke ratios are considered.

hairpins do not entrain as much fluid compared to the stronger hairpins produced at higher L/D (e.g. $L/D = 3$ as shown in figure 18*d*). As L/D increases beyond 3 (18*e*, *f*), each pulse creates more than one hairpin, which is then shed downstream. These hairpins are created on their natural time scale. In this case, the time scale of hairpin formation is approximately 2.5 (non-dimensionalized using U_p and D). This explains why V_{sc} increases till $L/D = 3$ and then remains constant. As long as the time scale of each pulse is larger than the required natural time scale for hairpin formation, more mixing will be observed. Again at these very low velocity ratios, duty cycle does not play much of a role if the velocity ratio is held constant. This is because the hairpins formed by each pulse are quickly swept away by the crossflow before they can interact with the subsequent hairpins. This is why the higher duty cycle is chosen to compare different stroke ratios. For very low duty cycles, e.g. 15 %, the interaction will be even less. It is found that the duty cycle does not have as large an impact at low velocity ratios as it does at high velocity ratios.

Similar results are observed for other low velocity ratios. Figure 20 shows scalar contours in the symmetry plane for velocity ratio of 1.0 at different stroke ratios. The duty cycle is kept constant at 75 %. Figure 20(*e*) shows the variation of V_{sc} for different stroke ratios. Again, note that the smaller stroke ratio ($L/D = 2.0$) in figure 20(*a*) results in weaker and smaller hairpins. Larger stroke ratios such as $L/D = 4.0, 6.0$ (figure 20*c*, *d*) yield stronger hairpins. The natural time scale at $r_{ring} = 1.0$ is approximately 3.0. The variation of V_{sc} in figure 20(*e*) is consistent with this physical behaviour.

6. Summary

Controlled simulations of fully modulated, laminar, pulsed jets in crossflow with square wave excitation are performed. Optimal pulsing conditions for maximum jet penetration and spread into the crossflow are examined. The evolution of pulsed jets in crossflow is interpreted in terms of the behaviour of single vortex rings in the presence of crossflow. The regime map in figure 1 (Sau & Mahesh 2008) for single

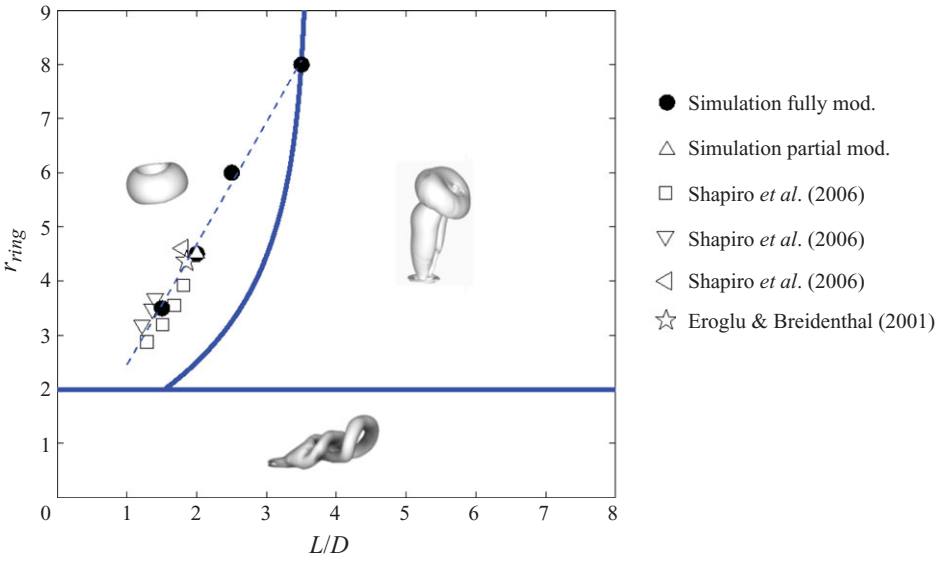

FIGURE 21. (Colour online) Optimal pulsing conditions from several experiments are plotted along with the optimal data from simulations. Note that the data collapse onto a curve.

vortex rings in crossflow shows that three different flow regimes exist, depending on the stroke ratio and ring velocity ratio. The pulse conditions (frequency, duty cycle) can be transformed into the ring parameters and the flow field can be interpreted using the regime map. Optimal pulsing conditions from all the simulations fall on a curve in the regime map. Also, data from a wide range of experiments (Eroglu & Breidenthal 2001; Shapiro *et al*. 2006) are interpreted in terms of their vortex rings, and optimal experimental conditions are seen to collapse on the same optimal curve in the regime map (figure 21).

The behaviour at high (greater than 2) and low (less than 2) velocity ratios is fundamentally different. For very high velocity ratios, the rings produced by successive pulses do not interact, and their behaviour is similar to that of single rings in crossflow. The optimal stroke ratio under these conditions marks the transition between a vortex ring and vortex ring with trailing column at a given ring velocity ratio (Sau & Mahesh 2008). The optimal stroke ratio for pulsed jets decreases as the ring velocity ratio decreases. However, as the ring velocity ratio decreases, successive rings begin to interact with each other and the overall penetration decreases. This interaction has the effect of shifting the optimal stroke ratio to the left of the transition curve. The jet apparently splits in two streams for stroke ratios, which produces upstream-tilted vortex rings without trailing column. This behaviour is observed at stroke ratios around the optimal conditions. The effect of duty cycle is examined. For very high values of duty cycle, the rings interact in the very near field irrespective of the stroke ratio and no optimum is found. As long as the duty cycle is low, an optimal penetration is obtained and this optimal stroke ratio does not change when duty cycle changes.

At very low ring velocity ratios, hairpin structures form, and are shed periodically. These hairpin structures form on a time scale that depends on velocity ratio and Reynolds number. Pulsed jet simulations at these low ring velocity ratios suggest that for optimal mixing, the time scale associated with each pulse should at least equal or be greater than the natural time scale of hairpin formation. Hence at very low velocity

ratios, large stroke ratios yield the most effective mixing. At very low velocity ratios, duty cycle does not affect the flow very much if the velocity ratio is held constant. Regardless of the duty cycle, the hairpins formed by each pulse are swept away by the crossflow before they can interact with each other.

The main contribution of this paper is to show how optimal pulsing conditions (at least for square wave pulsing) for jets in crossflow can be predicted in terms of the vortex rings produced by the pulsing. The regime map allows experimental control parameters such as stroke length, frequency, duty cycle, kinetic energy of fluctuations, etc. to be predicted by relating them to the ring stroke and velocity ratios. The collapse of data from a number of experiments and simulations is encouraging in the light of the wide scatter that optimal Strouhal numbers are known to display (Narayanan *et al*. 2003). Also, the effect of the crossflow is consistently accounted for in this paper and is not ignored (e.g. Johari 2006). The proposed idea is valid for both full and partial modulation, since ring parameters are based on the deviation of the velocity about the mean. Also, the regime map appears to be relatively robust, as demonstrated by the agreement between an ideal square waveform and a non-ideal experimental waveform. The regime map is therefore proposed as a promising approach to predict optimal conditions for pulsed jets in crossflow.

This work was supported by the Air Force Office of Scientific Research (AFOSR) under grant FA-9550-04-1-0064. Computer time was provided by the National Centre for Supercomputing Applications (NCSA), Minnesota Supercomputing Institute (MSI) and the San Diego Supercomputer Center (SDSC).

REFERENCES

Blossey, P., Narayanan, S. & Bewley, T. R. 2001 Dynamics and control of a jet in crossflow, direct numerical simulation and experiments. In *Proceedings of IUTAM Symposium on Turbulent Mixing Combustion* (ed. A. Pollard & S. Candel), pp. 45–56. Kluwer.

Chang, Y. K. & Vakili, A. D. 1995 Dynamics of vortex rings in crossflow. *Phys. Fluids* **7**, 1583–1597.

Eroglu, A. & Briedenthal, R. E. 2001 Structure, penetration and mixing of pulsed jets in crossflow. *AIAA J*. **39**, 417–423.

Gharib, M., Rambod, E. & Shariff, K. 1998 A universal time scale for vortex ring formation. *J. Fluid Mech*. **360**, 121–140.

Hermanson, J. C., Wahba, A. & Johari, H. 1998 Duty cycle effects on penetration of fully modulated, turbulent jets in crossflow. *AIAA J*. **36**, 1935–1937.

Johari, H. 2006 Scaling of fully pulsed jets in crossflow. *AIAA J*. **44**, 2719–2725.

Johari, H., Pacheco-Tougas, M. & Hermanson, J. C. 1999 Penetration and mixing of fully modulated jets in crossflow. *AIAA J*. **37**, 842–850.

Karagozian, A. R., Cortelezi, L. & Soldati, A. 2003 Manipulation and control of jets in crossflow. In *CISM Courses and Lectures, No. 439*, vol. 218. Springer.

Mahesh, K., Constantinescu, G. & Moin, P. 2004 A numerical method for large-eddy simulation in complex geometries. *J. Comput. Phys*. **197**, 215–240.

Margason, R. J. 1993 Fifty years of jet in crossflow research. In *AGARD Symp. on A jet in Crossflow*. AGARD CP-534.

Marshall, J. S. & Grant, J. R. 1994 Evolution and break-up of vortex rings in straining and shearing flows. *J. Fluid Mech*. **273**, 285–312.

M'Closkey, R. T., King, J. M., Cortelezzi, L. & Karagozian, A. R. 2002 The actively controlled jet in crossflow. *J. Fluid Mech*. **452**, 325–335.

Megerian, S., Davitian, J., Alves, L. S. De B. & Karagozian, A. R. 2007 Transverse-jet shear-layer instabilities. Part 1. Experimental studies. *J. Fluid Mech*. **593**, 93–129.

Muppidi, S. & Mahesh, K. 2008 Direct numerical simulation of passive scalar transport in transverse jets. *J. Fluid Mech*. **598**, 335–360.

Narayanan, S., Barooah, P. & Cohen, J. M. 2003 Dynamics and control of an isolated jet in crossflow. *AIAA J.* **14**, 2316–2330.

Sau, R. & Mahesh, K. 2007 Passive scalar mixing in vortex rings. *J. Fluid Mech.* **582**, 449–491.

Sau, R. & Mahesh, K. 2008 Dynamics and mixing of vortex rings in crossflow. *J. Fluid Mech.* **604**, 389–409.

Shapiro, S. R., King, J. M., Karagozian, A. R. & M'Closkey, R. T. 2003 Optimization of controlled jets in crossflow. *AIAA Paper* 2003-634.

Shapiro, S. R., King, J. M., Karagozian, A. R. & M'Closkey, R. T. 2006 Optimization of controlled jets in crossflow. *AIAA J.* **44**, 1292–1298.

Tomar, S., Arnaud, J. & Soria, J. 2004 Structure, penetration of a zero-net-mass-flux round jet in crossflow. *Tech Rep.* AFMC0024. In *Proceedings of 15th Australasian Fluid Mechanics Conference*, Sydney, Australia.

Vermeulen, P. J., Rainville, P. & Ramesh, V. 1992 Measurements of the entrainment coefficient of acoustically pulsed axisymmetric free air jets. *J. Engng Gas Turbines Power* **114** (2), 409–415.

Wu, J. M., Vakili, A. D. & Yu, F. M. 1988 Investigation of the interacting flow of non-symmetric jets in crossflow. *AIAA J.* **26**, 940–947.